

Absorption-Based Qubit Estimation in Discrete-Time Quantum Walks

Edgard P. M. Amorim,^{1,*} Lorena R. Cerutti,¹ O. P. de Sá Neto,² and M. C. de Oliveira^{3,†}

¹Departamento de Física, Universidade do Estado de Santa Catarina, 89219-710, Joinville, SC, Brazil

²Coordenação de Ciências da Computação, Universidade Estadual do Piauí, Parnaíba, PI 64202-220, Brazil

³Instituto de Física Gleb Wataghin, Universidade Estadual de Campinas, 13083-859, Campinas, SP, Brazil

(Dated: December 3, 2025)

We investigate state estimation in discrete-time quantum walks with a single absorbing boundary. Using a spectral approach, we obtain closed expressions for the escape probability as a function of the coin state and the boundary position, and their corresponding classical Fisher information for a simple absorption readout. Comparing with the single-copy quantum Fisher information shows a clear complementarity: near boundaries carry broad information about the population angle of the coin, whereas moderate or distant boundaries reveal phase-sensitive regions. Because a single boundary probes only one information direction, combining two boundary placements yields a full-rank Fisher matrix and tight joint Cramér–Rao bounds, while retaining a binary, tomography-free measurement. We outline an integrated-photonics implementation in which an on-chip sink realizes the absorber and estimate a substantial reduction in configuration count compared to mode-resolved qubit tomography. These results identify absorption in quantum walks as a simple and scalable primitive for coin-state metrology.

I. INTRODUCTION

Quantum walks are the quantum analogues of classical random walks, describing the coherent evolution of a quantum particle over a discrete or continuous set of positions [1]. In the discrete-time version, the walker possesses an internal degree of freedom—often called a coin space—that governs the direction of motion on the external position space. The total state of the system is therefore a vector in the tensor product of the coin and position Hilbert spaces. At each time step, the state evolves unitarily through the sequential action of two operators: a quantum coin operator, which performs a rotation in the coin subspace (analogous to tossing a coin in the classical walk), and a conditional shift operator, which displaces the walker according to the coin state. The combination of these operations leads to interference between different paths, producing probability distributions that differ markedly from their classical counterparts [2]. These interference effects give rise to distinctly quantum phenomena such as ballistic spreading, localization, and entanglement between the coin and position degrees of freedom, which make quantum walks a valuable framework for studying quantum transport, simulation, and algorithmic speed-ups [3–5].

Quantum walks have been extensively employed as the underlying mechanism for quantum search algorithms [6, 7] and they constitute a universal model for quantum computation, capable of implementing a complete set of logical gates [8, 9]. They also exhibit rich dynamical behavior: depending on the initial state and the sequence of quantum coins throughout the walk, they can display localization [10, 11], diffusive spreading with maximal entanglement between coin and position states [12], and soliton-like dynamics enabling high-fidelity state transfer [13–16]. Several physical platforms have been proposed and employed for their realization, including

photonic devices, trapped ions, and superconducting circuits [17–21].

Classical and quantum walkers behave differently in the presence of an absorbing boundary. Consider a simple symmetric *classical* random walk on $x \in \mathbb{Z}$ with an absorbing site placed one step from the starting position (e.g., start at $x = 0$, absorb at $x = 1$). With hop probability $p = 1/2$ to the left/right, the one-dimensional walk is *recurrent*: the hitting probability of any given site is 1. Consequently, the eventual absorption probability is $P_A = 1$ and the escape (survival) probability is $P_E = \lim_{n \rightarrow \infty} 1/2^n = 0$ (see, e.g., the recurrence discussion in [3]). By contrast, for a discrete-time quantum walk, the total absorption probability depends on the coin operator and the initial coin state. Interference generically leaves a nonzero amplitude on trajectories that never reach the boundary, yielding $P_E = 1 - P_A > 0$ even when the absorbing site is placed a finite distance from the initial position. This strict separation from the classical case—nonunit absorption on the half-line—has been analyzed in detail; see [22, 23].

A substantial literature exists on discrete-time quantum walks with absorbing boundaries. Different authors have employed distinct analytical techniques to obtain absorption (hitting) probabilities. Bach *et al.* derived closed-form expressions for walks with one and two static absorbing boundaries using, (i) a combinatorial approach based on generating functions and (ii) an eigenfunction (spectral) method built on the Fourier transform of the walk dynamics [22, 24]. Independently, Konno *et al.* obtained equivalent results via a path-counting approach grounded in a Feynman path-sum formulation [23]. Extensions include moving absorbing boundaries [25] and position-dependent (partially) reflecting boundaries [26].

While the counting and eigenfunction methods proceed differently, they are consistent and lead to the same absorption laws. The combinatorial framework enumerates path amplitudes directly in position space, through generating functions, while the eigenfunction method exploits that the step operator is diagonal in quasi-momentum, allowing a spectral decom-

* edgard.amorim@udesc.br

† marcos@ifi.unicamp.br

position of the time-evolved amplitudes. In both cases, the absorption probabilities are obtained from the long-time limit of the boundary-hitting amplitudes (or, equivalently, from the integrated boundary flux), yielding closed expressions for representative coins and initial states [22].

Our proposal is to address the following inference question: assuming we do not have access to the initial state of the walker, how much information do the (measurable) absorption/escape probabilities provide about that state? We adopt an estimation-theoretic point of view and quantify informativeness via the (classical) Fisher information. This type of binary measurement is particularly appealing in architectures where internal degrees of freedom or individual output modes are not experimentally resolved. In that setting, one can still probe the underlying coin qubit by repeating the walk many times and recording only whether the walker is absorbed or escapes. Throughout this work, we take a single-copy metrological perspective, in which each run of the walk encodes one copy of the unknown coin state and many independent repetitions are used to estimate its Bloch angles. The present strategy is highly relevant for integrated-photonics implementations using an on-chip sink, since it allows a substantial reduction in configuration count relative to full state tomography. For that end, we derive an analytical expression for the escape probability of a discrete-time quantum walk with an absorbing boundary, expressed as a function of the initial coin state (qubit) and the boundary position, using the spectral (eigenfunction) method in quasi-momentum space. Consequently, we obtain analytical Fisher informations for the coin parameters, benchmarked against the single-copy quantum Fisher information.

The paper is organized as follows. Section II summarizes the quantum-walk formalism in position and momentum representations. Section III reviews and adapts the eigenfunction approach of Ref. [22] to obtain analytical escape probabilities as functions of the coin parameters and boundary placement. Section IV develops the coin-state estimation framework and efficiencies. Section V remarks the relevance of the present findings for integrated photonic platforms with practical design rules and a photonics outlook. Lastly, Section VI presents the main conclusions.

II. QUANTUM WALKS

We consider a discrete-time quantum walk on the one-dimensional lattice. The quantum walker state belongs to the total Hilbert space $\mathcal{H} = \mathcal{H}_c \otimes \mathcal{H}_p$, where the two-dimensional coin space $\mathcal{H}_c = \text{span}\{|L\rangle, |R\rangle\}$ encodes an internal qubit and the position space $\mathcal{H}_p = \text{span}\{|j\rangle : j \in \mathbb{Z}\}$ encodes lattice sites, with $\langle j|j'\rangle = \delta_{j,j'}$. The walker is initialized at the origin with a general coin state, therefore, the joint initial state is

$$|\Psi(0)\rangle = [L(0,0)|L\rangle + R(0,0)|R\rangle] \otimes |0\rangle, \quad (1)$$

where $L(0,0) = \cos(\alpha/2)$ and $R(0,0) = e^{i\beta} \sin(\alpha/2)$ are the initial amplitudes with $\alpha \in [0, \pi]$ and $\beta \in [0, 2\pi]$ being

the usual polar and azimuth angles in the Bloch sphere representation [27]. The state evolves by $|\Psi(t)\rangle = U|\Psi(t-1)\rangle$, implying that after t time steps $|\Psi(t)\rangle = U^t|\Psi(0)\rangle$ for U constant over all the time and positions. The time evolution operator, $U = S(C \otimes \mathbb{1}_p)$, includes the biased Hadamard quantum coin,

$$C = \begin{bmatrix} \sqrt{\rho} & \sqrt{1-\rho} \\ \sqrt{1-\rho} & -\sqrt{\rho} \end{bmatrix}, \quad (2)$$

with a bias parameter $\rho \in [0, 1]$ (unbiased for $\rho = 1/2$), where $\mathbb{1}_p$ is the identity in the walker Hilbert space. It also includes the conditional displacement operator S , such that

$$\begin{aligned} S(|L\rangle \otimes |j\rangle) &= |L\rangle \otimes |j-1\rangle, \\ S(|R\rangle \otimes |j\rangle) &= |R\rangle \otimes |j+1\rangle, \end{aligned} \quad (3)$$

which moves the $|L\rangle$ ($|R\rangle$) amplitude to the left (right) neighboring lattice position.

To evaluate the escape probability of a quantum walker, we should take the asymptotic limit $t \rightarrow \infty$ of the probability over the positions out of the absorption barrier. However, since the U operator is non-diagonal, it is necessary to change the basis from \mathcal{H}_p to the dual k-space \mathcal{H}_k to diagonalize it. This space is spanned by the Fourier-transformed vectors $|k\rangle = \sum_j e^{ikj} |j\rangle$ with $k \in [-\pi, \pi]$. Then, the operator S_k is now diagonal

$$\begin{aligned} S_k(|L\rangle \otimes |k\rangle) &= e^{ik} |L\rangle \otimes |k\rangle, \\ S_k(|R\rangle \otimes |k\rangle) &= e^{-ik} |R\rangle \otimes |k\rangle. \end{aligned} \quad (4)$$

Therefore, the time-evolution operator U_k now reads

$$U_k = \begin{bmatrix} e^{ik} \sqrt{\rho} & e^{ik} \sqrt{1-\rho} \\ e^{-ik} \sqrt{1-\rho} & -e^{-ik} \sqrt{\rho} \end{bmatrix}. \quad (5)$$

The diagonalization of U_k gives the eigenvalues

$$\lambda_{k\pm} = \sqrt{\rho} \left(i \sin k \pm \sqrt{\cos^2 k - 1 + \frac{1}{\rho}} \right) = e^{-i\omega_{k\pm}}, \quad (6)$$

with $\omega_{k+} = -\sin^{-1}(\sqrt{\rho} \sin k)$ and $\omega_{k-} = \pi - \omega_{k+}$. These eigenvalues are associated to the following eigenstates $\Psi_{k\pm} = (A_{k\pm}, B_{k\pm})^T$, such that

$$\begin{aligned} A_{k\pm} &= \frac{1}{\sqrt{2N}} \sqrt{1 \pm \frac{\cos k}{\sqrt{1/\rho - \sin^2 k}}}, \\ B_{k\pm} &= \pm \frac{e^{-ik}}{\sqrt{2N}} \sqrt{1 \mp \frac{\cos k}{\sqrt{1/\rho - \sin^2 k}}}, \end{aligned} \quad (7)$$

with a condition of normalization $|A_{k\pm}|^2 + |B_{k\pm}|^2 = 1/N$, so that the sum of the probabilities is equal to 1 over any N lattice positions. The term $\pm e^{-ik}$ in the Eq. (7) is just an arbitrary phase to guarantee that $A_{k\pm}$ are real and positive [22].

III. ABSORPTION BARRIER

Let us now introduce the recurrence equations considering an absorption barrier placed on $j = M$, where $M > 0$. Note that for the positions $j < M - 1$, we have the recurrence equations for a biased Hadamard walk with no barrier influence,

$$\begin{bmatrix} L(j, t) \\ R(j, t) \end{bmatrix} = \begin{bmatrix} \sqrt{\rho}L(j+1, t-1) + \sqrt{1-\rho}R(j+1, t-1) \\ \sqrt{1-\rho}L(j-1, t-1) - \sqrt{\rho}R(j-1, t-1) \end{bmatrix}. \quad (8)$$

For $j \geq M$, as our walker starts on $j = 0$, the amplitudes arrive at the barrier only coming from left to right. After the amplitudes cross the barrier, they do not return to the opposite direction. These amplitudes represent the part of the state absorbed by the barrier. Therefore, the barrier behaves like an identity operator,

$$\begin{bmatrix} L(j, t) \\ R(j, t) \end{bmatrix} = \begin{bmatrix} L(j+1, t-1) \\ R(j-1, t-1) \end{bmatrix}. \quad (9)$$

At last, for $j = M - 1$, note that the amplitude $L(M, t - 1)$ originates from the barrier at the right, while the amplitude $R(M - 1, t)$ comes from the Hadamard coin at the left, therefore

$$\begin{bmatrix} L(M-1, t) \\ R(M-1, t) \end{bmatrix} = \begin{bmatrix} L(M, t-1) \\ \sqrt{1-\rho}L(M-2, t-1) - \sqrt{\rho}R(M-2, t-1) \end{bmatrix}. \quad (10)$$

As discussed above, when the quantum walker reaches the barrier and no longer returns, the amplitude $L(M - 1, t)$ must vanish for all times t . However, the eigenstates $\Psi_{k\pm}$ of the system do not satisfy this boundary condition. To enforce $L(M - 1, t) = 0$, we express the initial condition as a superposition of eigenfunctions such that the contributions from different wave numbers k share the same frequency ω , allowing them to interfere destructively at the barrier. This condition can be conveniently realized through the *method of images*, illustrated in Fig. 1. In this approach, two walkers are considered symmetrically positioned with respect to the boundary site $j = M - 1$. The real walker is located at $j = 0$, and a mirror walker is placed at $j = 2(M - 1)$. This symmetric construction ensures that the superposition of the real and mirror walkers satisfies the boundary constraint [22, 26].

After employing the method of images, we arrive at the following solution,

$$\begin{bmatrix} L(j, t) \\ R(j, t) \end{bmatrix} = \sum_{k \in (-\frac{\pi}{2}, \frac{\pi}{2})} e^{-i\omega_{k\pm} t} \left\{ C_{k\pm} \begin{bmatrix} A_{k\pm} \\ B_{k\pm} \end{bmatrix} e^{ikj} + C_{(\pi-k)\pm} \begin{bmatrix} A_{(\pi-k)\pm} \\ B_{(\pi-k)\pm} \end{bmatrix} e^{i(\pi-k)j} + D_{k\pm} \begin{bmatrix} A_{k\pm} \\ B_{k\pm} \end{bmatrix} e^{ik[j-2(M-1)]} + D_{(\pi-k)\pm} \begin{bmatrix} A_{(\pi-k)\pm} \\ B_{(\pi-k)\pm} \end{bmatrix} e^{i(\pi-k)[j-2(M-1)]} \right\}, \quad (11)$$

where $\omega_{k\pm} = \omega_{(\pi-k)\pm}$. Then, $L(M - 1, t) = 0$ implies

$$D_{k\pm} = -e^{i\pi(M-1)} C_{(\pi-k)\pm} \frac{A_{(\pi-k)\pm}}{A_{k\pm}}. \quad (12)$$

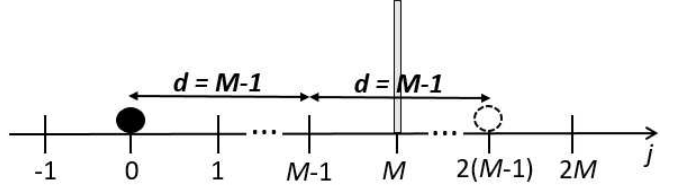


FIG. 1: Schematic representation of the *method of images*. The real walker (solid circle) starts at $j = 0$, while a mirror walker (open circle) is placed at $j = 2(M - 1)$. Both walkers are symmetrically positioned around the boundary site, each at a distance $d = M - 1$. The superposition of their wave functions ensures that the amplitude $L(M - 1, t)$ vanishes at the boundary for all times.

Therefore, inside the domain $j < M$ the solution reads

$$\begin{bmatrix} L(j, t) \\ R(j, t) \end{bmatrix} = \sum_{k \in (-\frac{\pi}{2}, \frac{\pi}{2})} \left\{ \begin{bmatrix} A_{k\pm} \\ B_{k\pm} \end{bmatrix} e^{ikj} F_{k\pm} + \begin{bmatrix} A_{(\pi-k)\pm} \\ B_{(\pi-k)\pm} \end{bmatrix} e^{i(\pi-k)j} G_{k\pm} \right\}, \quad (13)$$

with

$$\begin{aligned} F_{k\pm} &= C_{k\pm} - C_{(\pi-k)\pm} \frac{A_{(\pi-k)\pm}}{A_{k\pm}} e^{i(\pi-2k)(M-1)}, \\ G_{k\pm} &= C_{(\pi-k)\pm} - C_{k\pm} \frac{A_{k\pm}}{A_{(\pi-k)\pm}} e^{-i(\pi-2k)(M-1)}, \end{aligned} \quad (14)$$

and taking the local initial condition $(L(0, 0), R(0, 0))^T$ we conclude [22, 26] that

$$C_{k\pm} = A_{k\pm} L(0, 0) + B_{k\pm}^* R(0, 0). \quad (15)$$

The solution of Eq. (13) consists of a superposition of wave functions with components going to the left and right. The components on the left are the only ones that will be on the physical domain $j < M$ in the long time limit. These components survive the barrier and compose the escape probability of the particle,

$$P_E(M) = \sum_{k \in (-\frac{\pi}{2}, \frac{\pi}{2})} |F_{k+}(M)|^2 + |G_{k-}(M)|^2. \quad (16)$$

Replacing Eqs. (7) and (15) into Eq. (14), we arrive at $G_{k-} = F_{k+}^*$ to rewrite the escape probability as

$$P_E(M) = \sum_{k \in (-\frac{\pi}{2}, \frac{\pi}{2})} 2|F_{k+}(M)|^2, \quad (17)$$

with

$$\begin{aligned} F_{k+}(M) &= \frac{L(0, 0)}{A_{k+}} \left(A_{k+}^2 - e^{i(\pi-2k)(M-1)} A_{k-}^2 \right) \\ &+ R(0, 0) A_{k-} \left(e^{ik} + e^{i(\pi-2k)(M-1)} e^{-ik} \right). \end{aligned} \quad (18)$$

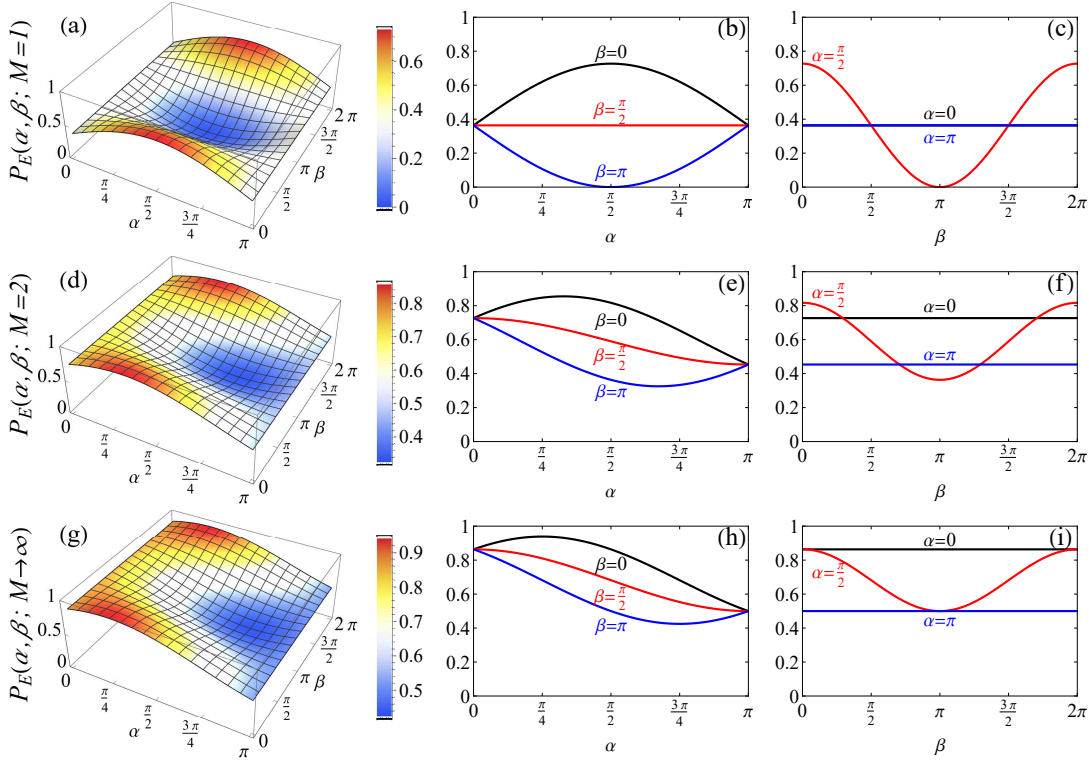


FIG. 2: Escape probability $P_E(\alpha, \beta; M)$ as a function of the Bloch angles (α, β) for barrier positions (a)–(c) $M = 1$, (d)–(f) $M = 2$, and (g)–(i) $M \rightarrow \infty$. The first column shows the surface $P_E(\alpha, \beta; M)$ for each case, while the second and third columns display one-dimensional cuts of these surfaces for $\alpha, \beta = 0$ (black), $\pi/2$ (red), and π (blue). Note that in panel (c) the curves for $\alpha = 0$ and $\alpha = \pi$ coincide.

After converting the sum of the Eq. 17 to an integral, we solve the resulting integrals over k assuming a Hadamard-walk ($\rho = 1/2$). We follow the steps of the Ref. [22]. Our interest relies only on assessing the escape probability of a walker positioned closest and farthest possible to the absorption barrier. Then, we obtain the escape probability $P_E(M)$ towards $j \rightarrow -\infty$ for the cases with $M = 1$ to 5 and $M \rightarrow +\infty$. Note that the boundary imposed by $L(M-1, t) = 0$ restricts the initial qubit on $j = 0$ to have $L(0, 0) = 0$ with a barrier on $M = 1$. This restriction could be easily managed by evolving the state for one time step by hand [22]. For instance, taking an initial state $(\cos(\alpha/2) |L\rangle + e^{i\beta} \sin(\alpha/2) |R\rangle) \otimes |0\rangle$, after one step with a neighbor barrier, it evolves to the unab-sorbed state $(\cos(\alpha/2) + e^{i\beta} \sin(\alpha/2)) |L\rangle \otimes |-1\rangle$. The escape probability of such a state is equivalent to $P_E(2)_L$ where the subindex L indicates a walk starting from a qubit $|L\rangle$, we have then $P_E(1) = (1 + \sin \alpha)^2 P_E(2)_L / 2$. All these manipulations above drive us to the following closed expressions of the escape probability,

$$P_E(\alpha, \beta) = \xi_1 \cos^2\left(\frac{\alpha}{2}\right) + \xi_2 \sin^2\left(\frac{\alpha}{2}\right) + \xi_3 \cos\left(\frac{\alpha}{2}\right) \sin\left(\frac{\alpha}{2}\right) \cos \beta, \quad (19)$$

whose the constants ξ_i are listed in Table I for selected values of M . Figure 2 displays the escape probability $P_E(\alpha, \beta; M)$ obtained from Eq. (19) using the coefficients ξ_i from Table I

for barrier positions $M = 1$, $M = 2$, and $M \rightarrow \infty$. For $M = 1$, the escape probability has a symmetric profile, as shown in the first row of Fig. 2 [panels (a)–(c)]. This indicates that qubits on the northern hemisphere of the Bloch sphere have the same escape probability as the corresponding qubits on the southern hemisphere. Moreover, only for $M = 1$ does the escape probability reduce to

$$P_E(\alpha, \beta; M=1) = \left(1 - \frac{2}{\pi}\right) (1 + \sin \alpha \cos \beta), \quad (20)$$

which vanishes at $(\alpha, \beta) = (\pi/2, \pi)$. A Hadamard coin applied to this particular qubit at site $j = 0$ yields the state $|R\rangle$, and the conditional displacement operator moves it to the right, where it is completely absorbed by the barrier at

TABLE I: Calculated values for ξ_1 , ξ_2 , and ξ_3 .

M	ξ_1	ξ_2	ξ_3
1	$1 - \frac{2}{\pi}$	$1 - \frac{2}{\pi}$	$2 - \frac{4}{\pi}$
2	$2 - \frac{4}{\pi}$	$3 - \frac{8}{\pi}$	$3 - \frac{8}{\pi}$
3	$4 - \frac{10}{\pi}$	$13 - \frac{118}{3\pi}$	$11 - \frac{100}{3\pi}$
4	$14 - \frac{124}{3\pi}$	$65 - \frac{608}{3\pi}$	$53 - \frac{496}{3\pi}$
5	$66 - \frac{614}{3\pi}$	$341 - \frac{16046}{15\pi}$	$277 - \frac{13936}{15\pi}$
∞	$\frac{3}{2} - \frac{2}{\pi}$	$\frac{1}{2}$	$1 - \frac{2}{\pi}$

$j = 1$. For $M > 1$, the escape probability becomes asymmetric: qubits with a larger amplitude of $|L\rangle$ have a higher escape probability than those with a larger amplitude of $|R\rangle$, and this difference becomes more pronounced as M increases. This behavior reflects the fact that the absorbing barrier is placed at a positive position $j > 0$. These configurations, corresponding to $M = 1$ (nearest boundary), $M = 2$ (moderate distance), and $M \rightarrow \infty$ (larger distance), will serve as our starting point for estimating the qubit parameters via the Fisher information in the next section.

IV. COIN STATE ESTIMATION

In natural systems such as quantum walks, we have intrinsic statistical properties influenced by observable and unobservable physical quantities. The observable physical quantities are all those that can be measured. In contrast, the unobservable ones influence the curvature of the probability of detection in the system, and they are defined as parameters. We view absorption readout as a binary measurement with success probability $P_E(\alpha, \beta; M)$ given by Eq. (19). For N independent runs of the walk at a fixed boundary position M , the number of escapes k follows a binomial law with likelihood

$$\mathcal{L}(\alpha, \beta) \propto P_E(\alpha, \beta; M)^k [1 - P_E(\alpha, \beta; M)]^{N-k}. \quad (21)$$

We can estimate the initial state of a quantum walk constructed inside a box by measuring $P_E(\alpha, \beta; M)$. For a single parameter $\theta \in \{\alpha, \beta\}$, the per-trial (classical) Fisher information $F_\theta(\alpha, \beta; M) \equiv F_\theta(\alpha, \beta)$ [28] is given by

$$F_\theta(\alpha, \beta) = \frac{[\partial_\theta P_E(\alpha, \beta; M)]^2}{P_E(\alpha, \beta; M) [1 - P_E(\alpha, \beta; M)]}. \quad (22)$$

With N i.i.d. trials, the Cramér–Rao bound (CRB) [29–31] for any unbiased estimator θ reads

$$\text{Var}(\theta) \geq \frac{1}{N F_\theta(\alpha, \beta)}, \quad (23)$$

showing that a larger $F_\theta(\alpha, \beta)$ yields a tighter (smaller) Cramér–Rao lower bound for $\text{Var}(\theta)$, and therefore allowing, in principle, more precise estimation of θ . Using (19), we obtain

$$F_\alpha(\alpha, \beta) = \frac{[(\xi_2 - \xi_1) \sin \alpha + \xi_3 \cos \alpha \cos \beta]^2}{f(\alpha, \beta) [2 - f(\alpha, \beta)]}, \quad (24)$$

and

$$F_\beta(\alpha, \beta) = \frac{[\xi_3 \sin \alpha \sin \beta]^2}{f(\alpha, \beta) [2 - f(\alpha, \beta)]}, \quad (25)$$

with $f(\alpha, \beta) = \xi_2 + \xi_1 - (\xi_2 - \xi_1) \cos \alpha + \xi_3 \sin \alpha \cos \beta$, where ξ_i depend on M as seen in Table I.

Figure 3 shows the Fisher information F_α and F_β as functions of the Bloch angles (α, β) of the initial qubit. For $M = 1$, we have an outstanding estimate for α when $\beta = \pi$, except at $\alpha = \pi/2$. This means that all initial qubits whose

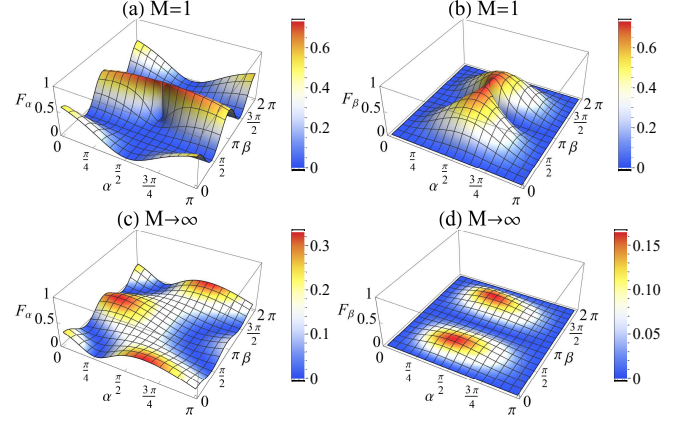


FIG. 3: Fisher information F_α (left column) and F_β (right column) as functions of the initial qubit (α, β) for the barrier positions (a)–(b) $M = 1$ and (c)–(d) $M \rightarrow \infty$.

amplitudes of $|L\rangle$ and $|R\rangle$ have opposite phases ($\beta = \pi$) can be accurately estimated, provided these amplitudes are different ($\alpha \neq \pi/2$). This behavior corroborates the symmetry discussed above for $P_E(\alpha, \beta; M = 1)$: qubits on the northern hemisphere of the Bloch sphere have the same escape probability as their counterparts on the southern hemisphere. Only for the qubit $(\alpha, \beta) = (\pi/2, \pi)$, which is completely absorbed by the barrier at $j = 1$, is the estimate poor. Similarly, we obtain an excellent estimate for β when $\alpha = \pi/2$, except at $\beta = \pi$ and approximately for $\beta < \pi/2$ and $\beta > 3\pi/2$, where F_β decreases monotonically to zero. In this case, the situation is reversed: the amplitudes of $|L\rangle$ and $|R\rangle$ are equal (qubits on the Bloch sphere's equator); however, as the relative phase between $|L\rangle$ and $|R\rangle$ approaches zero or π , the estimate becomes poor. Finite values of $M > 1$ are remarkably similar to $M \rightarrow \infty$ where we have a distinct behavior in the estimates. In such a case, we have *hot spots* corresponding to two particular qubits ($P_E \approx 0.77$), in which a fine estimate can also be made.

Since both coin parameters are unknown in general, it is natural to consider the Fisher information *matrix* (per trial)

$$\mathcal{F}(\alpha, \beta; M) = \frac{1}{P_E(1 - P_E)} \begin{bmatrix} (\partial_\alpha P_E)^2 & \partial_\alpha P_E \partial_\beta P_E \\ \partial_\alpha P_E \partial_\beta P_E & (\partial_\beta P_E)^2 \end{bmatrix}, \quad (26)$$

so for N independent trials we have $N \mathcal{F}$. Its determinant and conditioning quantify identifiability of (α, β) at a given M and explain the *hot spots* seen in Fig. 3. Combining data from multiple boundary placements $\{M_\ell\}$ adds information,

$$\mathcal{F}_{\text{tot}}(\alpha, \beta) = \sum_\ell \mathcal{F}(\alpha, \beta; M_\ell), \quad (27)$$

which mitigates the poor sensitivity of F_β at $M = 1$ and improves joint estimation via an increased $\det \mathcal{F}_{\text{tot}}$.

Now, instead of performing the quantum walk, we check Eq. (1) by direct measurement, whose quantum Fisher information (QFI) is given by

$$H_\theta = 4 \left[\langle \partial_\theta \Psi_\theta(0) | \partial_\theta \Psi_\theta(0) \rangle - |\langle \Psi(0) | \partial_\theta \Psi_\theta(0) \rangle|^2 \right]. \quad (28)$$

For the pure initial coin state of Eq. (1), parameterized by (α, β) , the single-copy QFI under optimal measurements is $H_\alpha = 1$ and $H_\beta = \sin^2 \alpha$.

A convenient performance metric is the (dimensionless) efficiency,

$$\eta_\theta(\alpha, \beta; M) = \frac{F_\theta(\alpha, \beta; M)}{H_\theta} \leq 1, \quad (29)$$

which quantifies how close absorption readout comes to the ultimate bound without requiring full tomography (note η_β is defined only where $H_\beta > 0$).

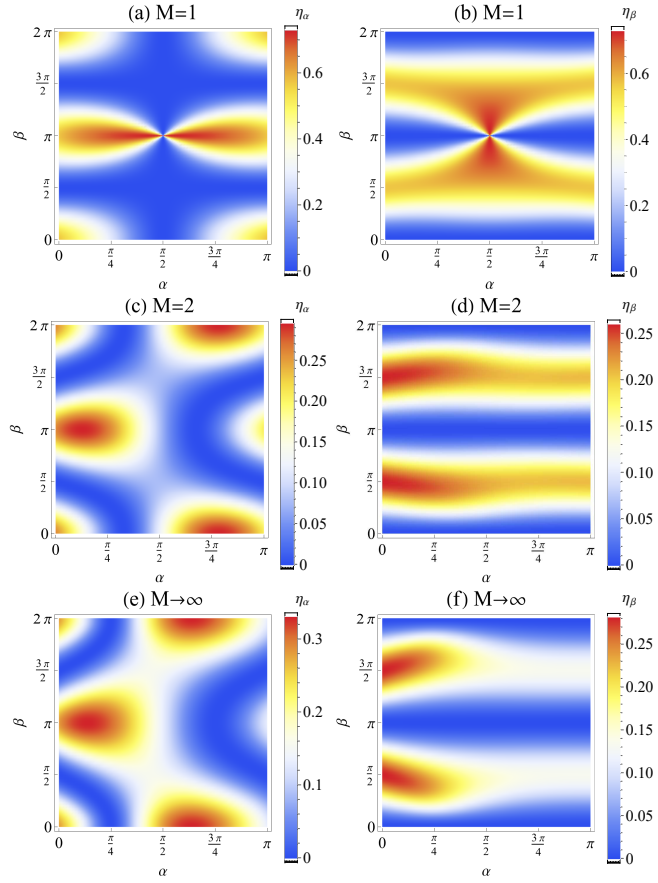


FIG. 4: Efficiency of absorption readout relative to the quantum limit. Left column: $\eta_\alpha(\alpha, \beta; M) = F_\alpha/H_\alpha$; right column: $\eta_\beta(\alpha, \beta; M) = F_\beta/H_\beta$. Top, middle, and bottom rows correspond to boundary placements $M = 1$, $M = 2$, and $M \rightarrow \infty$, respectively. Axes: $\alpha \in [0, \pi]$ (horizontal), $\beta \in [0, 2\pi]$ (vertical). Color encodes per-trial efficiency (dimensionless), capped at the 99th percentile to avoid saturation near singular sets where $P_E(1 - P_E) \rightarrow 0$. For $M = 1$, η_α is broadly high except near $\alpha = \pi/2$, while η_β is largely suppressed. As M increases, phase-sensitive “hot spots” emerge in η_β (notably around $\alpha \approx \pi/2$ and $\beta \approx \pi/2, 3\pi/2$), and η_α becomes more structured. These complementary patterns motivate combining two boundary placements to obtain well-conditioned joint estimation of (α, β) and tighter Cramér–Rao bounds at fixed N .

Figure 4 displays the efficiencies $\eta_\alpha(\alpha, \beta; M) = F_\alpha/H_\alpha$ (left column) and $\eta_\beta(\alpha, \beta; M) = F_\beta/H_\beta$ (right column) for three boundary placements at $M = 1$, $M = 2$, and $M \rightarrow \infty$. Two robust consequences explain most features: (i) η_β must vanish along $\beta \in \{0, \pi\}$ and near $\alpha \in \{0, \pi\}$ because either $\sin \beta = 0$ or $H_\beta = \sin^2 \alpha = 0$; (ii) η_α is suppressed near $\alpha = \pi/2$ unless the interference term $\xi_3 \cos \beta$ compensates the zero of $\cos \alpha$. In addition, both efficiencies decay close to the singular sets $P_E \in \{0, 1\}$, where the Bernoulli variance vanishes and the binary measurement carries no information.

For the nearest boundary ($M = 1$), $\xi_1 = \xi_2$ and $\xi_3 > 0$, so $F_\alpha \propto (\xi_3 \cos \alpha \cos \beta)^2$. The map of η_α exhibits a broad plateau of high efficiency across most (α, β) , with a dip centered at $\alpha = \pi/2$. In contrast, $\eta_\beta \propto (\sin \alpha \sin \beta)^2$ is generically small, showing only weak ridges near $\alpha \simeq \pi/2$ and $\beta \simeq \pi/2, 3\pi/2$ (tempered by the Bernoulli factor). Operationally, a single near boundary is excellent for estimating the population angle α but information-poor for the phase β .

At moderate distances (e.g. $M = 2$), $(\xi_2 - \xi_1) \neq 0$ and ξ_3 is reduced, producing interference between the $\sin \alpha$ and $\cos \alpha \cos \beta$ terms in F_α . The η_α landscape remains strong but loses uniformity, while η_β develops localized *hot spots* near $\alpha \approx \pi/2$ and $\beta \approx \pi/2, 3\pi/2$, where $|\sin \alpha \sin \beta|$ is maximal and P_E stays away from $\{0, 1\}$. In the limit ($M \rightarrow \infty$), both $(\xi_2 - \xi_1)$ and ξ_3 remain $\mathcal{O}(1)$, sharpening the phase-sensitive islands in η_β and making η_α more structured. These trends confirm a clean complementarity: near boundaries favor α , far boundaries expose β .

Because for a single M the per-trial Fisher information matrix is $\mathcal{F} \propto g g^\top$ (with $g = (\partial_\alpha P_E, \partial_\beta P_E)$), it has rank 1, so joint estimation is informed only along the gradient direction. Consequently, one should combine two (or more) boundary placements, as in Eq. (27), chosen so that the corresponding sensitivity directions are not colinear at the operating point. A practical and effective choice is $M_1 = 1$ (high η_α across a broad region) together with a moderate or large M_2 (phase-sensitive *hot spots* in η_β). This pairing yields a well-conditioned \mathcal{F}_{tot} , tightening the matrix Cramér–Rao bound at fixed resources N .

V. ABSORPTION READOUTS AND FULL STATE TOMOGRAPHY

We should remark the relevance of the present findings for integrated photonic platforms, as they already realize discrete-time quantum walks in reconfigurable waveguide arrays and multiport interferometers, with single- and two-photon versions widely demonstrated [32–34]. In such devices, characterization typically relies on full quantum state tomography of path/polarization qubits (or qudits), which demands many measurement settings and phase-stable reconfigurations [35] (see also Ref. [36] for another strategy). The present proposal offers a lighter alternative: implement the absorbing boundary as a controllable on-chip *sink* (e.g., evanescent coupling to a lossy bus or integrated detector) and read out only a binary outcome (escaped vs. absorbed). Since the sensitivity patterns for α and β are complementary across M , two boundary

placements suffice to approach a sizable fraction of the QFI without reconstructing the full output state.

To show the advantage of the present proposal in contrast to full state tomography, let us consider a T -step 1D walk with support over $K \approx 2T+1$ spatial modes. A coin-qubit tomography that is local and mode-resolved requires at least 3 projective settings (Pauli X, Y, Z) per mode, i.e., $S_{\text{tomo}} \sim 3K$ distinct configurations; with N detection events per configuration, the total sample count scales as $N_{\text{tomo}} \sim 3KN$. In contrast, absorption readout at s boundary placements (typically $s = 2$) needs only $S_{\text{abs}} = s$ configurations and $N_{\text{abs}} \sim sN$ samples for similar statistical confidence along the FI directions. For a concrete example, $T = 50$ implies $K \approx 101$; then $S_{\text{tomo}} \sim 303$ versus $S_{\text{abs}} = 2$, i.e., $\gtrsim 150\times$ fewer reconstructions, while also avoiding phase-stable interferometric settings. Although exact constants depend on platform details (losses, detector efficiency, finite-time corrections), this scaling highlights the practical value of absorption-based estimation for on-chip quantum-walk characterization.

To summarize, a minimal, resource-efficient strategy would be to: (i) choose a near boundary to estimate α robustly over wide regions of (α, β) ; (ii) add a second, more distant boundary to harvest phase information around the identified *hot spots*; and (iii) pool the two datasets to obtain a well-conditioned Fisher matrix and precise joint estimates with modest statistics. Note that our analysis assumes a Hadamard coin ($\rho = 1/2$), perfect absorption, single-particle dynamics, and the long-time limit. Decoherence, partial reflectivity, and state-preparation errors will modify the efficiencies quantitatively but preserve the qualitative structure (symmetry-enforced zeros, phase-sensitive ridges, and the $P_E(1 - P_E)$ singular sets).

VI. CONCLUSIONS

We derived closed-form expressions for the escape probability of discrete-time quantum walks with a single absorbing

boundary, explicitly as functions of the Bloch angles (α, β) of the initial coin state and the boundary position M . From these we obtained analytic Fisher informations F_α and F_β and benchmarked them against the single-copy quantum Fisher information, $H_\alpha = 1$ and $H_\beta = \sin^2 \alpha$. The resulting efficiency maps $\eta_\alpha = F_\alpha/H_\alpha$ and $\eta_\beta = F_\beta/H_\beta$ reveal a clear, operational complementarity: *near* boundaries (e.g., $M = 1$) are broadly informative about the population angle α , whereas *moderate/large* distances (e.g., $M = 2$ and $M \rightarrow \infty$) create phase-sensitive islands informative about β . Because the per-trial Fisher matrix at fixed M has rank 1, combining two boundary placements turns the information full rank and tightens the joint Cramér–Rao bound while retaining the simplicity of a binary (absorption) readout.

To conclude, we also discussed that absorption measurements furnish a metrological primitive for integrated quantum-walk devices: with two boundary placements and modest statistics, one can approach quantum-limited precision for (α, β) while bypassing full tomography, enabling fast device bring-up, in-situ calibration, and lightweight performance monitoring in scalable photonic architectures.

ACKNOWLEDGMENTS

E. P. M. Amorim thanks J. Longo for the manuscript revision. This work was supported by Conselho Nacional de Desenvolvimento Científico e Tecnológico - CNPq through grant No. 409673/2022-6. M. C. de Oliveira acknowledges the financial support of the National Institute of Science and Technology for Applied Quantum Computing (INCT-CQA) through CNPq process No. 408884/2024-0 and FAPESP, through the Center for Research and Innovation on Smart and Quantum Materials (CRISQuaM) process No. 2013/07276-1.

[1] Y. Aharonov, L. Davidovich, and N. Zagury, Phys. Rev. A **48**, 1687 (1993).
[2] K. Pearson, Nature **72**, 294 (1905).
[3] J. Kempe, Contemp. Phys. **44**, 307 (2003).
[4] S. E. Venegas-Andraca, Quantum Inf. Process. **11**, 1015 (2012).
[5] R. Portugal, *Quantum Walks and Search Algorithms* (Springer, New York, 2013).
[6] N. Shenvi, J. Kempe, and K. B. Whaley, Phys. Rev. A **67**, 052307 (2003).
[7] A. Tulsi, Phys. Rev. A **78**, 012310 (2008).
[8] A. M. Childs, Phys. Rev. Lett. **102**, 180501 (2009).
[9] N. B. Lovett, S. Cooper, M. Everitt, M. Trevers, and V. Kendon, Phys. Rev. A **81**, 042330 (2010).
[10] R. Vieira, E. P. M. Amorim, and G. Rigolin, Phys. Rev. A **89**, 042307 (2014).
[11] L. I. da S. Teles and E. P. M. Amorim, Braz. J. Phys. **51**, 911 (2021).
[12] R. Vieira, E. P. M. Amorim, and G. Rigolin, Phys. Rev. Lett. **111**, 180503 (2013).
[13] A. C. Orthey and E. P. M. Amorim, Phys. Rev. A **99**, 032320 (2019).
[14] H. S. Ghizoni and E. P. M. Amorim, Braz. J. Phys. **49**, 168 (2019).
[15] R. Vieira, G. Rigolin, and E. P. M. Amorim, Phys. Rev. A **104**, 032224 (2021).
[16] J. P. Engster, R. Vieira, E. I. Duzzioni, and E. P. M. Amorim, Quantum Inf. Process. **23**, 103 (2024).
[17] T. Nitsche, S. Barkhofen, R. Kruse, L. Sansoni, M. Štefaňák, A. Gábris, V. Potoček, T. Kiss, I. Jex, and C. Silberhorn, Science Advances **4**, eaar6444 (2018), <https://www.science.org/doi/10.1126/sciadv.aar6444>.
[18] F. Zähringer, G. Kirchmair, R. Gerritsma, E. Solano, R. Blatt, and C. F. Roos, Phys. Rev. Lett. **104**, 100503 (2010).
[19] J. Lozada-Vera, A. Carrillo, O. P. D. S. Neto, J. K. Moqadam, M. D. Lahaye, and M. C. de Oliveira, EPJ Quantum Technology 2016 3:1 3, 9 (2016).

- [20] J. Khatibi Moqadam, M. C. de Oliveira, and R. Portugal, Phys. Rev. B **95**, 144506 (2017).
- [21] J. Wang and K. Manouchehri, *Physical Implementation of Quantum Walks* (Springer, Berlin, 2013).
- [22] E. Bach, D. Coppersmith, M. P. Goldschen, R. Joynt, and J. Watrous, J. Comput. Syst. Sci. **69**, 562 (2004).
- [23] N. Konno, T. Namiki, T. Soshi, and A. Sudbury, J. Phys. A: Math. Gen. **36**, 241 (2003).
- [24] E. Bach and L. Borisov, “Absorption probabilities for quantum walks on the line,” (2009), arXiv:0901.4349 [quant-ph].
- [25] L. C. Kwek and Setiawan, Phys. Rev. A **84**, 032319 (2011).
- [26] F. Wang, P. Zhang, Y. Wang, R. Liu, H. Gao, and F. Li, Phys. Lett. A **381**, 65 (2017).
- [27] M. A. Nielsen and I. L. Chuang, *Quantum Computation and Quantum Information*, 10th ed. (Cambridge University Press, Cambridge, 2010).
- [28] R. A. Fisher, Math. Proc. Camb. Philos. Soc. **22**, 700 (1925).
- [29] H. Cramér, *Mathematical Methods of Statistics* (Princeton University Press, Princeton, NJ, 1946).
- [30] C. R. Rao, Bull. Calcutta Math. Soc. **37**, 81 (1945).
- [31] C. R. Rao, *Selected Papers of C. R. Rao*, edited by S. Das Gupta (Wiley, New York, 1994).
- [32] A. Peruzzo, M. Lobino, J. C. F. Matthews, N. Matsuda, A. Politi, K. Poulios, X. Zhou, Y. Lahini, N. Ismail, K. Wörhoff, Y. Bromberg, Y. Silberberg, M. G. Thompson, and J. L. O’Brien, Science **329**, 1500 (2010).
- [33] L. Sansoni, F. Sciarrino, G. Vallone, P. Mataloni, A. Crespi, R. Ramponi, and R. Osellame, Physical Review Letters **108**, 010502 (2012).
- [34] L. Neves and G. Puentes, Entropy **20**, 731 (2018).
- [35] D. F. V. James, P. G. Kwiat, W. J. Munro, and A. G. White, Physical Review A **64**, 052312 (2001).
- [36] F. E. S. Steinhoff and M. C. de Oliveira, Phys. Rev. A **82**, 062308 (2010).